IR (Nujol)3377、1621、1610cm^{-1}

APCI-MS　m/z 563[M+H]$^{+}$

^{18}F-THK-5117 の標識合成

サイクロトロン HM12(住友重機械工業)で加速した 12 MeV の陽子ビームを同位体純度 98%以上の[^{18}O]H_2O に照射して $^{18}F^{-}$を製造した。続いてその溶液を陰イオン交換樹脂(AG1-X8)に通して $^{18}F^{-}$を樹脂上に捕捉し、33 mM K_2CO_3 溶液で溶出させた。この $^{18}F^{-}$含有 K_2CO_3 水溶液を褐色バイアルにとり、Kryptofix222 (16 mg)、アセトニトリル(2.3 mL)を加えてオイルバス(110℃)で加熱しながら He ガスを吹き付け、水を共沸させながらアセトニトリルを完全に除去した。さらにアセトニトリル(1.5 mL)を加え同様に加熱条件下でアセトニトリルを除去する操作を 2 回繰り返して、バイアル内を無水の状態にした。そこに、標識前駆体(3.0 mg)を溶解した DMSO 溶液(0.70 mL)を加え、オイルバス(110℃)で 10 分間加熱攪拌した。その後、反応溶液に塩酸(2M、0.2 mL)を添加してさらに 110℃で 3 分間反応させた後、酢酸カリウム溶液(4M、0.1 mL)と蒸留水(7.0 mL)で反応溶液を希釈して Sep-Pak tC18 カートリッジ(Waters)にロードし、蒸留水でカートリッジを洗浄後、粗生成物をエタノールで溶出した。もっとも放射能の高いエタノール画分を蒸留水で希釈してセミ分取高速液体クロマトグラフィー(カラム: Inertsil ODS-4 (10×250 mm)、移動相: MeCN/NaH_2PO_4 (20 mM) = 45/55、流速: 5.0 mL/min)にかけ、^{18}F-THK-5117 由来の放射性ピークを分取した。

C. 研究結果

目的とする THK-5117 の標品については、図 1 に示したスキームに従って合成した。2,6-ジヒドロキノリンを出発原料として、途中鈴木-宮浦反応を経由し、6 工程で目的とする化合物の合成に成功した。いずれの反応でも良好な収率で生成物を得ることができた。

THK-5117 のフッ素 18 標識体を合成するために用いる前駆化合物として、図 2 に示したスキームに従って、化合物 17 を合成した。化合物 2 を出発原料として、鈴木-宮浦反応で 2-アリールキノリン骨格を構築し、次いでアミノメチル化反応を経て化合物 11 を合成した。11 の保護基を除去した後、脱離基としてトシルオキシ基を有するプロパノール構造を導入(化合物 15)し、その OH 基を THP で保護して、メチルアミノ基の保護基を除去して目的とする化合物 17 を合成した。この合成においても、各反応ステップの収率は良好であった。

この標識前駆体を使用して、図 3 反応識で示した条件で、^{18}F-THK-5117 の標識合成を行った。その結果、6 回の標識合成の平均収率(減衰補正値)は 44％となり、分取

HPLC 完了までの標識合成時間は 54 分であった。

D. 考察

本研究では、新しいフッ素 18 標識タウ画像化プローブとして、THK-5117 の標品およびその標識前駆体合成を行った。そしてフッ素 18 標識体の合成を検討したところ、短い合成時間で、再現性良く良好な収率で目的物を合成し、純度良く精製できたことから、臨床での利用を考えた場合でも十分実用性のある標識合成法を確立できたと考えられる。

E. 結論

新規フッ素 18 標識タウプローブ候補 ^{18}F-THK-5117 の実用的合成法を確立した。

F. 研究発表

1．論文発表

1) Shidahara M, Tashiro M, Okamura N, Furumoto S, Furukawa K, Watanuki S, Hiraoka K, Miyake M, Iwata R, Tamura H, Arai H, Kudo Y, Yanai K: Evaluation of the biodistribution and radiation dosimetry of the 18F-labelled amyloid imaging probe [18F]FACT in humans.EJNMMI Res. 3.32-41. 2013

2) Okamura N,Furumoto S,Harada R,Tago T,Yoshikawa T,Fodero-Tavoletti M,Mulligan R S,Villemagne V L, Akatsu H,Yamamoto T, Arai H, Iwata R,Yanai K., Kudo Y: Novel 18F-labeled arylquinoline derivatives for non-invasive imaging of tau pathology in Alzheimer's disease. Journal of Nuclear Medicine. (Accepted) 2013

3) Furumoto S, Okamura N, Furukawa K, Tashiro M, Ishikawa Y, Sugi K, Tomita N, Waragai M, Harada R, Tago T, Iwata R, Yanai K, Arai H, Kudo Y: A (18)F-Labeled BF-227 Derivative as a Potential Radioligand for Imaging Dense Amyloid Plaques by Positron Emission Tomography. Mol Imaging Biol. (Accepted) 2013

4) Niu K,Guo H,Guo Y,Ebihara S,Asada M,Ohrui T,Furukawa K,Ichinose M,Yanai K,Kudo Y,Arai H,Okazaki T,Nagatomi R.: Royal jelly prevents the progression of sarcopenia in aged mice in vivo and in vitro. Journal of Gerontology:Biological Sciences. (Accepted) 2013

5) Harada R, Okamura N, Furumoto S, Tago T, Maruyama M, Higuchi M, YosikawaT, Arai H, Iwata R, Kudo Y, Yanai K: Comparison of the binding characteri stics of [(18)F]THK-523 and other amyloid imaging tracers to Alzheimer's disease patholopgy. Eur J Nucl Med Mol Imaging. 40. 125-132. 2013

6) Tomita N, Furukawa K, Okamura N, Tashiro M, Une K, Furumoto S, Iwata R, Yanai K, Kudo Y, Arai H: Brain accumulation of amyloid β protein visualized by positoron emission tomography and BF-227 in Alzheimer's disease patients with or without diabetes mellitus. Geriatr Gerontol Int. 13. 215-221. 2013

7) Villemagne V L, Furumoto S, Fodero-Tavoletti M, Harada R, Mulligan R S, Kudo Y, Masters C L, Yanai K, Rowe C C, Okamura N: The challenges of tau imaging. Future Neurology. 7. 409-421. 2012

8) Furukawa K, Ikeda S, Okamura N, Tashiro M, Tomita N, Furumoto S, Iwata R,Yanai K, Kudo Y, Arai H : Cardiac positron-emission tomography images with an amyloid-specific tracer in familial transthyretin-related systemic amyloidosis. Circulation. 125. 556-557. 2012

9) 工藤幸司、荒井啓行： 脳アミロイドーシス.編集 田村和夫. In"血液症候群（第 2 版）別冊 日本臨床" 株式会社日本臨床社.大阪市.pp648-652. 2013

2．学会発表

海外学会発表

1) Harada R, Okamura N, Furumoto S,

Tago T, Yoshikawa , Arai H, Yanai K, Kudo Y : Binding of the novel pet tracer [18Ｆ]ＴＨＫ-5117 reflects the amount of tau in Alzheimer's Disease Brain. The 11th International conference on Alzheimer's & Parkinson's diseases.2013 年 3 月 6 日～10 日（3 月 8 日ポスターセッション）イタリア（フローレンス）

2) Okamura N,Furumoto S,Harada R,Fodero-Tavoletti M.T,Mulligan R.S,Masters C.L,Yanai K., Kudo Y, Rowe C.C,Villemagne V.L.: In vivo tau imaging in Alzheimer's Disease using [18Ｆ]ＴＨＫ-5105. The 11th International conference on Alzheimer's & Parkinson's diseases.2013 年 3 月 6 日～10 日（3 月 8 日ポスターセッション）イタリア（フローレンス）

3) Okamura N, Furumoto S, Harada R, Tago T, Fodero-Tavoletti M, Villemagne VL, Iwata R, Arai H, Yanai K, Kudo Y: [18F]THK-5105 and [18F]THK-5117 as possible PET probes for in vivo detection of tau pathology in Alzheimer's disease.Human Amyloid Imaging 2013. (2013 年 1 月 16 日～18 日)米国・マイアミ

4) Furumoto S, Kawauchi T, Okamura N,T ago T, Harada R ,Zhang MR, Higuchi M, Yanai K, Iwata R, Kudo Y: Novel fluorine-18labeled benzothizaole derivatives for amyloid imaging by PET. Annual Congress of the European Association of Nuclear Medicine 2012 (2012 年 10 月 26 日～10 月 31 日)MiCo-Milano Congressi (イタリア・ミラノ)

5) Harada R,Okamura N,Furumoto S,Yoshikawa T,Arai H,Kudo Y,Yanai K: Wavelength-dependent selective detection of tau pathology in Alzheimer's disease using a novel fluorescent probe THK-1188. Alzheimer's Association International Conference2012(２０１２年７月１４日～１９日)バンクーバーコンベンションセンター（カナダ）

6) Suzuki M,Tomita N,Okamura N,Furukawa K,Kudo Y,Arai H: The relationships between memory impairment and dense beta-amyloid deposition reflected by BF-227. Alzheimer's Association International Conference2012(２０１２年７月１４日～１９日)バンクーバーコンベンションセンター（カナダ）

7) Villemagene V L, Furumoto S,Fodero-Tavoletti M T,Mulligan R S,Hodges J,Piguet O,Pejoska S、Kudo Y,Masters C L,Yanai K,Rowe C C,Okamura N: In vivo tau imaging in Alzheimer's disease and other dementias. Alzheimer's Association International Conference2012(２０１２年７月１４日～１９日)バンクーバーコンベンションセンター（カナダ）

8) Okamura N,Furumoto S,Harada R,Fodero-Tavoletti M,Villemagene V,Iwata R,Yanai K,Kudo Y: Novel 18F-labeled quinoline derivatives for in vivo detection of tau pathology in Alzheimer's disease. Alzheimer's Association International Conference2012(２０１２年７月１４日～１９日)バンクーバーコンベンションセンター（カナダ）

9) Okamura N, Furukawa k, Tashiro M, Furumoto S, Harada R, Arai H, Kudo Y, Yanai K: [11C]BF-227 PET study in patients with dementia with Lewy bodies. 第 59 回米国核医学会議 SNM 2012 (2012 年 6 月 12 日)米国・マイアミ

国内学会発表

1) 原田龍一、岡村信行、古本祥三、多胡哲郎、吉川雄朗、荒井啓行、岩田錬、谷内一彦、工藤幸司:タウイメージングプローブ候補化合物 18Ｆ標識アリールキノリン誘導体の前臨床評価.第 86 回 日本薬理学会年会.2013 年 3 月 21 日～23 日（3 月 22 日 オーラルセッション）福岡国際会議場

2) 岡村信行、原田龍一、古本祥三、吉川雄朗、工藤幸司、谷内一彦: 生体内のアミロイド線維を非侵略的に検出する近赤外蛍光プローブX65の開発. 第86回 日本薬理学会年会
2013 年 3 月 21 日～23 日(3 月 23 日ポスター発表）福岡国際会議場

3) 古本祥三、岡村信行、多胡哲郎、原田龍一、石川洋一、岩田錬、谷内一彦、工藤幸司
2-アリールキノリンを母核とするフッ素18標識タウ画像化プローブ.第52回日本核医学会学術総会(2012年10月11日～13日) ロイトン札幌・さっぽろ芸術文化の館

4) 工藤幸司、丸山将浩: 特異的プローブによるタウ及びAβ蓄積メカニズムの解明. 分子イメージング研究戦略推進プログラム 成果発表シンポジウム 2012 (２０１２年８月１日) 神戸国際会議場メインホール

5) 岡村信行、古本祥三、工藤幸司: 特異的プローブによるタウ及びAβ蓄積メカニズムの解明（タウイメージング）.分子イメージング研究戦略推進プログラム 成果発表シンポジウム 2012 (２０１２年８月１日) 神戸国際会議場メインホール

6) 古本祥三、岡村信行、工藤幸司: 特異的プローブによるタウ及びAβ蓄積メカニズムの解明(アミロイド　イメージング) 分子イメージング研究戦略推進プログラム 成果発表シンポジウム 2012 (２０１２年８月１日) 神戸国際会議場メインホール

7) 原田龍一、岡村信行、古本祥三、吉川朗、工藤幸司、谷内一彦: アルツハイマー病病理像検出のための光ｲﾒｰｼﾞﾝｸﾞ. 分子イメージング研究戦略推進プログラム 成果発表シンポジウム 2012 (２０１２年８月１日) 神戸国際会議場メインホール

8) 原田龍一、岡村信行、古本祥三、吉川雄朗、谷内一彦、工藤幸司
アルツハイマー病病理像を生体画像化するための光イメージングプローブの開発. 第7回日本分子イメージング学会総会・学術集会.(2012年5月24-25日) アクトシティ浜松（静岡県）

9) 岡村信行、古本祥三、原田龍一、多胡哲郎、岩田錬、谷内一彦、工藤幸司: 新規18F標識プローブTHK-5105によるタウ蛋白の生体イメージング. 第7回日本分子イメージング学会総会・学術集会.(2012年5月24-25日)アクトシティ浜松（静岡県）

9) 原田龍一、岡村信行、古本祥三、吉川雄朗、谷内一彦、工藤幸司: 波長依存性蛍光プローブによるアミロイド・タウの選択的検出. 第7回日本分子イメージング学会総会・学術集会.(2012年5月24-25日)アクトシティ浜松（静岡県）

G．知的財産権の出願・登録状況（予定も含む）

１．特許取得
次ページの出願が国際公開されました。
（2013年4月以降、次ページ特許を複数の国に各国移行させる予定）

２．実用新案登録
なし

３．その他
なし

特許出願状況

以下の出願が国際公開されました。

発明の名称	発明者	出願登録区分	出願番号（出願日）	出願区分	出願国	登録番号（登録日）	メモ
タウイメージングプローブ	工藤幸司 岡村信行 古本祥三	出願	PCT/JP2011/074930（2011年10月28日）	PCT	日本		**国際公開番号** WO2012/057312 **公開日** 2012年5月3日

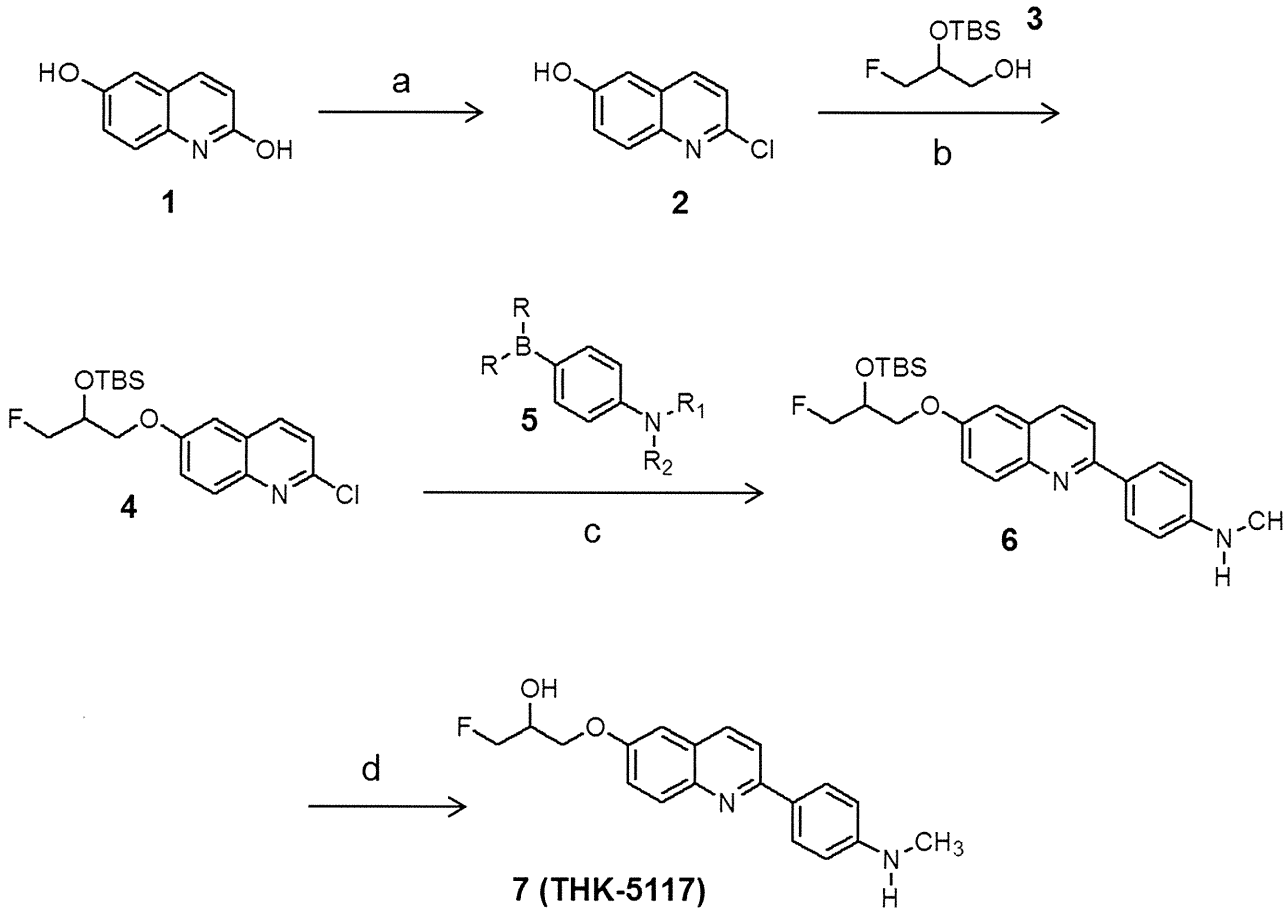

図1　THK-5117 の合成経路. 試薬と条件: (a) $SOCl_2$, DMF, room temperature (rt); (b) PPh_3, DIAD, THF, rt; (c) $Pd(PPh_3)_4$, K_2CO_3, DME, H_2O, 80℃; (d) (i) TBAF, THF, rt. (ii) TFA, $CHCl_3$, rt.

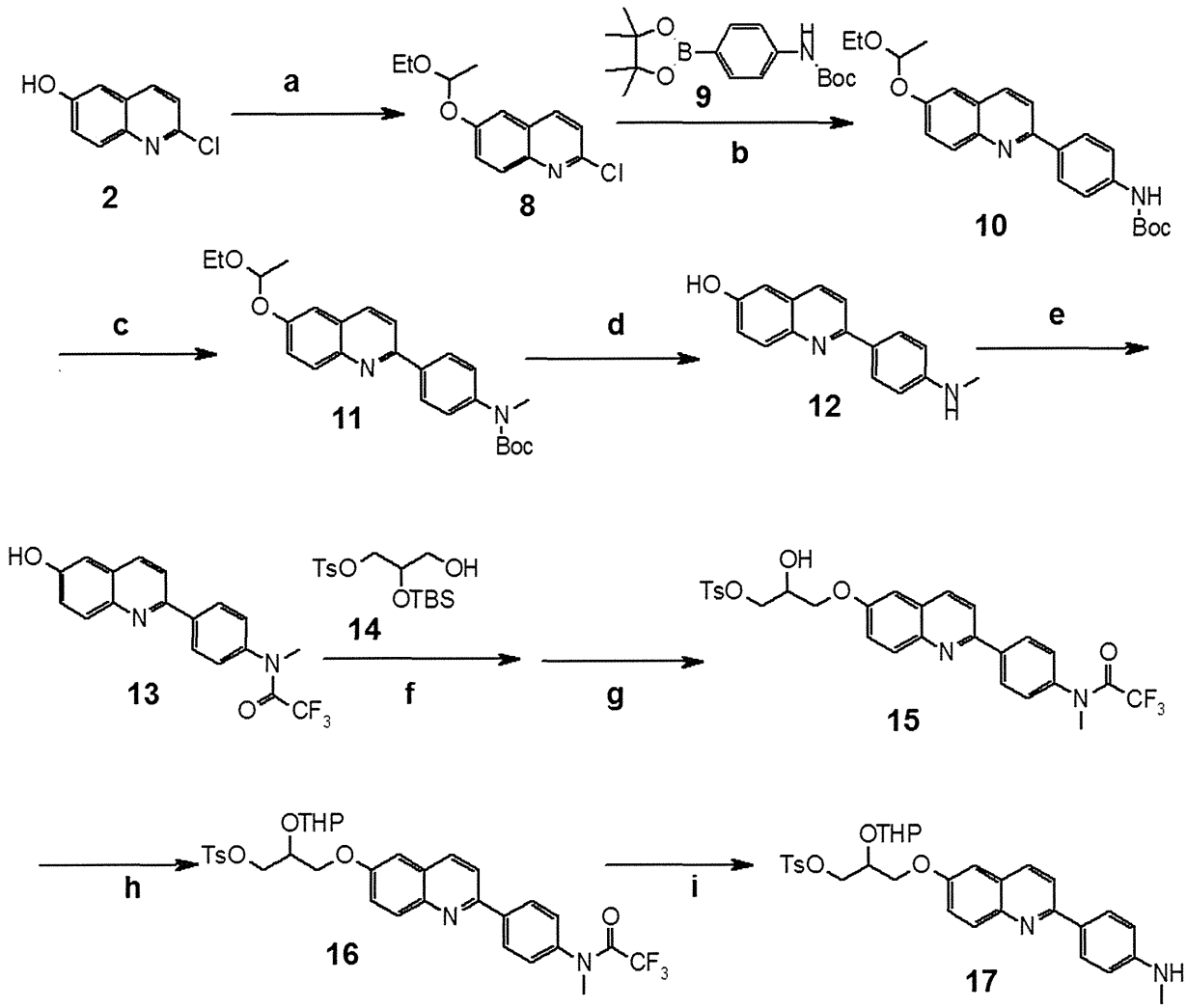

図２　THK-5117 の標識前駆体の合成: (a) Ethyl vinyl ether, Py·TsOH, THF, room temperature (rt); (b) $Pd(PPh_3)_4$, K_2CO_3, DME, H_2O, 80°C; (c) NaH, CH_3I, DMF, 0°C; (d) TFA, $CHCl_3$, rt; (e) $(CF_3CO)_2O$, TEA, CH_2Cl_2, 0°C; (f) 2-(TBS-oxy)-3-tosyloxy-1-propanol, PPh_3, DIAD, THF, rt; (f) TFA, H_2O, $CHCl_3$, rt; (h) DHP, $TsOH·H_2O$, CH_2Cl_2, rt; (i) LiOH, THF/H_2O, 0 °C.

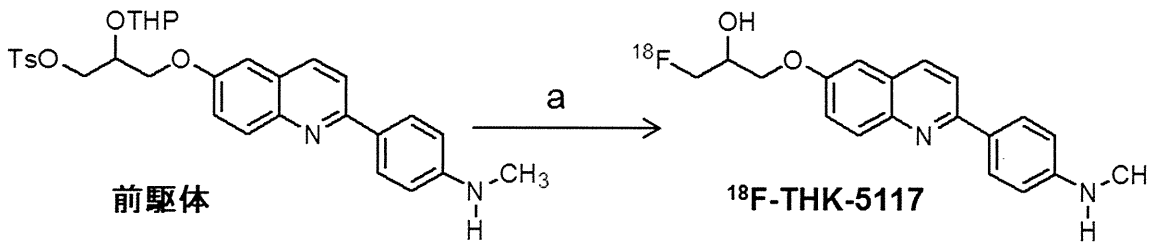

図３　標識合成. 試薬と条件: (a) (i) [^{18}F]KF/Kryptfix222, DMSO, 110°C, 10 min. (ii) aq. HCl, 110°C, 3 min.

研究成果の刊行に関する一覧表

研究成果の刊行に関する一覧表

雑誌

発表者氏名	論文タイトル名	発表誌名	巻号	ページ	出版年
Shidahara M, Tashiro M, Okamura N, Furumoto S, Furukawa K, Watanuki S, Hiraoka K, Miyake M, Iwata R, Tamura H, Arai H, Kudo Y, Yanai K	Evaluation of the biodistribution and radiation dosimetry of the ^{18}F-labelled amyloid imaging probe [^{18}F]FACT in humans	EJNMMI Res	3	32-41	2013
Okamura N,Furumoto S,Harada R,Tago T,Yoshikawa T,Fodero-Tavoletti M,Mulligan R S,Villemagne V L, Akatsu H,Yamamoto T, Arai H, Iwata R,Yanai K., Kudo Y	Novel 18F-labeled arylquinoline derivatives for non-invasive imaging of tau pathology in Alzheimer's disease	Journal of Nuclear Medicine		Accepted	2013
Furumoto S, Okamura N, Furukawa K, Tashiro M, Ishikawa Y, Sugi K, Tomita N, Waragai M, Harada R, Tago T, Iwata R, Yanai K, Arai H, Kudo Y	A (18)F-Labeled BF-227 Derivative as a Potential Radioligand for Imaging Dense Amyloid Plaques by Positron Emission Tomography	Mol Imaging Biol		Accepted	2013
Niu K,Guo H,Guo Y,Ebihara S,Asada M,Ohrui T,Furukawa K,Ichinose M,Yanai K,Kudo Y,Arai H,Okazaki T,Nagatomi R.	Royal jelly prevents the progression of sarcopenia in aged mice in vivo and in vitro	Journal of Gerontology:Biological Sciences		Accepted	2013
Harada R, Okamura N, Furumoto S, Tago T, Maruyama M, Higuchi M, YosikawaT, Arai H, Iwata R, Kudo Y, Yanai K	Comparison of the binding characteri stics of [(18)F]THK-523 and other amyloid imaging tracers to Alzheimer's disease patholopgy	Eur J Nucl Med Mol Imaging	40	125-132	2013
Tomita N, Furukawa K, Okamura N, Tashiro M, Une K, Furumoto S, Iwata R, Yanai K, Kudo Y, Arai H	Brain accumulation of amyloid β protein visualized by positoron emission tomography and BF-227 in Alzheimer's disease patients with or without diabetes mellitus	Geriatr Gerontol Int	13	215-221	2013
Villemagne V L, Furumoto S, Fodero-Tavoletti M, Harada R, Mulligan R S, Kudo Y, Masters C L, Yanai K, Rowe C C, Okamura N	The challenges of tau imaging	Future Neurology	7	409-421	2012

Furukawa K, Ikeda S, Okamura N, Tashiro M, Tomita N, Furumoto S, Iwata R,Yanai K, Kudo Y, Arai H	Cardiac positron-emission tomography images with an amyloid-specific tracer in familial transthyretin-related systemic amyloidosis	Circulation	125	556-557	2012

研究成果の刊行に関する一覧表

書籍

著者氏名	論文タイトル名	書籍全体の編集者名	書籍名	出版社名	出版地	出版年	ページ
工藤幸司 荒井啓行	脳アミロイドーシス	田村和夫	血液症候群（第2版） 別冊 日本臨床	株式会社日本臨床社	大阪市	2013	648 -652

研究成果の刊行物・別刷

Shidahara et al. EJNMMI Research 2013, 3:32
http://www.ejnmmires.com/content/3/1/32

EJNMMI Research
a SpringerOpen Journal

ORIGINAL RESEARCH Open Access

Evaluation of the biodistribution and radiation dosimetry of the ^{18}F-labelled amyloid imaging probe [^{18}F]FACT in humans

Miho Shidahara[1,2*], Manabu Tashiro[2], Nobuyuki Okamura[3], Shozo Furumoto[3], Katsutoshi Furukawa[4], Shoichi Watanuki[2], Kotaro Hiraoka[2], Masayasu Miyake[2], Ren Iwata[5], Hajime Tamura[1], Hiroyuki Arai[4], Yukitsuka Kudo[6] and Kazuhiko Yanai[2,3]

Abstract

Background: The biodistribution and radiation dosimetry of the ^{18}F-labelled amyloid imaging probe ([^{18}F] FACT) was investigated in humans.

Methods: Six healthy subjects (three males and three females) were enrolled in this study. An average of 160.8 MBq of [^{18}F] FACT was intravenously administered, and then a series of whole-body PET scans were performed. Nineteen male and 20 female source organs, and the remainder of the body, were studied to estimate time-integrated activity coefficients. The mean absorbed dose in each target organ and the effective dose were estimated from the time-integrated activity coefficients in the source organs. Biodistribution data from [^{18}F] FACT in mice were also used to estimate absorbed doses and the effective dose in human subjects; this was compared with doses of [^{18}F] FACT estimated from human PET data.

Results: The highest mean absorbed doses estimated using human PET data were observed in the gallbladder (333 ± 251 μGy/MBq), liver (77.5 ± 14.5 μGy/MBq), small intestine (33.6 ± 30.7 μGy/MBq), upper large intestine (29.8 ± 15.0 μGy/MBq) and lower large intestine (25.2 ± 12.6 μGy/MBq). The average effective dose estimated from human PET data was 18.6 ± 3.74 μSv/MBq. The highest mean absorbed dose value estimated from the mouse data was observed in the small intestine (38.5 μGy/MBq), liver (25.5 μGy/MBq) and urinary bladder wall (43.1 μGy/MBq). The effective dose estimated from the mouse data was 14.8 μSv/MBq for [^{18}F] FACT.

Conclusions: The estimated effective dose from the human PET data indicated that the [^{18}F] FACT PET study was acceptable for clinical purposes.

Keywords: Positron emission tomography, Radiation dosimetry, Amyloid imaging, MIRD, [^{18}F] FACT

Background

Amyloid beta imaging

Deposits of amyloid β (Aβ) plaque are one of the pathological observations in patients with Alzheimer's disease (AD); Aβ deposition progresses at an earlier point than the current clinical diagnostic point for this disease [1]. For earlier diagnosis of AD and the evaluation of treatment efficacy, *in vivo* amyloid imaging using positron emission tomography (PET), which provides quantitation and visualisation of Aβ deposition in the brain, is useful. Therefore, several Aβ-binding probes dedicated for PET imaging have been developed [2,3].

Most of these PET Aβ ligands are ^{11}C-labelled compounds (physical half life ($T_{1/2}$), 20 min), and ^{18}F-labelled agents are being increasingly investigated owing to their long half life ($T_{1/2}$, 109.7 min). The long $T_{1/2}$ of ^{18}F enables several PET scans to be carried out from a single synthesis of labelled agent and also enables its commercial distribution to any PET facility. On the other hand, the longer the $T_{1/2}$ of the radioisotope gets, the greater is the radiation

* Correspondence: shidahara@med.tohoku.ac.jp
[1]Division of Medical Physics, Tohoku University School of Medicine, 2-1 Seiryo-machi, Aoba-ku, Sendai 980-8575, Japan
[2]Division of Cyclotron Nuclear Medicine, Cyclotron Radioisotope Center, Tohoku University, Sendai 980-8578, Japan
Full list of author information is available at the end of the article

dose exposure for the PET subject for the same administered dose of radioligand.

Importance of radiation dosimetry

For subjects undergoing PET, internal radiation exposure is inevitable, and the radiation dose delivered is proportional to the level of radioactivity of the injected radioligand and the number of injections. In the case of amyloid imaging, subjects often have multiple PET scans for diagnostic or therapeutic longitudinal monitoring of Aβ aggregation in the brain. Therefore, estimation of the radiation dose exposure from each PET radioligand and the use of well-balanced PET scan protocols taking into consideration subject risk and benefit are important.

Estimation of the internal radiation dose requires a time series measurement of the biodistribution of the injected radioligand. There are two ways to establish the biodistribution of a radioligand in humans: one is to extrapolate from data obtained in animal experiments [4] and the other is to use data from a clinical whole-body PET study [5]. Data extrapolated from animal experiments have been used to estimate clinical radiation dose. However, Sakata et al. reported that in some radioligands, there were considerable differences in organ dose or kinetics between human and animal experiments and that a whole-body PET study would be desirable for the initial clinical evaluation of new PET radioligands [6].

Previous biodistribution and dosimetry study for PET amyloid imaging

Recently, radiation dose exposures from several PET amyloid imaging agents have been reported using clinical whole-body PET scans. One of the popular amyloid ligands, Pittsburgh compound B ([^{11}C]PIB), has been extensively investigated with regard to its kinetics in the human body, and its effective radiation dose was found to be 4.74 μSv/MBq on average [7]. For ^{18}F-labelled PET amyloid radioligands, effective doses in humans have been reported as follows: ^{18}F-AV-45, 13 and 19.3 μSv/MBq [8,9]; ^{18}F-GE067, 33.8 μSv/MBq [10]; and ^{18}F-BAY94-9172, 14.7 μSv/MBq [11].

Aim of the present study

Fluorinated amyloid imaging compound ([^{18}F]FACT) is an ^{18}F-labelled amyloid imaging agent developed at Tohoku University [12]. Kudo and colleagues at this university have previously developed a ^{11}C amyloid imaging agent named [^{11}C]BF-227 [3]. [^{18}F]FACT is derived from [^{11}C]BF-227 by reducing its lipophilicity in order to reduce the nonspecific binding in the brain; AD patients showed significantly higher uptake of [^{18}F]FACT in the neocortex region relative to controls [12]. However, the biodistribution of [^{18}F]FACT in humans has not yet been investigated.

In the present study, the radiation dosimetry and biodistribution of [^{18}F]FACT was investigated in healthy elderly subjects who are the target group for PET amyloid imaging. In order to determine the discrepancy in the estimated radiation dose between human and animal experiments, biodistribution studies in mice involving [^{18}F]FACT were also conducted.

Methods

Subjects

PET studies were performed in three healthy male and in three healthy female volunteers (mean age ± standard deviation (SD), 76.3 ± 3.2 years). Subject characteristics are shown in Table 1. Both height and weight varied over a wide range (146 to 175 cm and 39 to 74 kg, respectively). All subjects were Japanese and were free of somatic and neuropsychiatric illness, as determined by clinical history and physical examination; one male subject (no. 1) had undergone a previous surgical operation involving gallbladder removal.

This study was approved by the Ethics Committee on Clinical Investigations of Tohoku University School of Medicine and was performed in accordance with the Declaration of Helsinki. Written informed consent was obtained from all subjects after a complete description of the study had been made.

Radiochemistry and radioligand purity

Figure 1 shows the chemical structure of ^{18}F-FACT. The radiochemical purity of the radioligand in the present clinical study ranged from 97.8% to 98.7% (mean ± SD, 98.33 ± 0.42%). The specific radioactivity ranged from 30.6 to 347.7 GBq/μmol at the time of injection (mean ± SD, 139.9 ± 116.2 GBq/μmol).

PET study

All whole-body PET studies were performed using a SET-2400W scanner (Shimadzu Inc., Kyoto, Japan) in two-dimensional (2D) mode [13]. The PET scanner acquired 63 image slices at a centre-to-centre interval of 3.125 mm and had a spatial resolution of 3.9 mm full width at half maximum (FWHM) and a *Z*-axis resolution of 6.5 mm FWHM at centre field of view [13].

An overview of scan protocols is shown in Figure 2. Four emission scans and two transmission scans (before administration and intermediate emission scans) using a ^{68}Ge/^{68}Ga source were performed, with the exception of subject no. 1 who had three emission scans. In the present series of PET studies and in other research projects, a 15-min PET brain scan using three-dimensional (3D) mode was performed after the first emission scan. At 2 min after intravenous administration of 142 to 180 MBq [^{18}F]FACT (mean ± SD, 160.8 ± 14.8 MBq; injection mass, 0.77 ± 0.66 ng), a series of whole-body PET

Table 1 Information regarding the human subjects

	Sex	Age (years)	Height (m)	Weight (kg)	BMI (kg/m^2)	History
Subject number						
1	M	77	1.59	61.2	24.2	Surgical removal of gallbladder
2	M	78	1.62	65	24.8	-
3	M	77	1.75	74	24.2	-
4	F	70	1.46	39	18.3	-
5	F	77	1.56	60.2	26.1	-
6	F	79	1.55	56	23.3	-
Mean ± 1 SD		76.3 ± 3.2	1.58 ± 0.75	59.2 ± 11.6	23.5 ± 2.7	

scans were performed. The schedule for the first and second transmission scans and the first, second, third and fourth emission scans was as follows: 6 positions × 4 min (24 min), 6 positions × 4 min (24 min), 6 positions × 3 min (18 min), 6 positions × 3 min (18 min), 6 positions × 3 min (18 min), and 6 positions × 4 min (24 min), respectively. The starting time of the second emission scan was different for each subject and was on average 55 min after the start of injection with a 5-min SD. The time gap between bed positions was 5 s. All emission data were reconstructed using OS-EM with iteration 16 and subset 2 after attenuation correction. Scatter correction was not performed because of the use of 2D mode data acquisition. The cross calibration factor of the scanner (Bq per ml/cps per voxel) was determined once per week using a cylindrical water phantom (25-cm length and 20-cm inner diameter) filled with ^{18}F solutions and by measuring the sample activity of the ^{18}F solutions at the well counter (BSS-3: Shimadzu Co., Ltd., Kyoto, Japan) [14].

Urination was controlled before, after and during the series of PET studies. In particular, during (15 min after the end of the first emission scan) and after the PET scans, subjects were asked to void. The volume and radioactivity levels of their urine samples were measured using a calibrated well counter.

MRI study

All subjects underwent T1-weighted magnetic resonance imaging (MRI) scans using a Signa 1.5-T machine (General Electric Inc., Milwaukee, WI, USA) within a week of the PET scans. For each position (brain, chest, abdomen and epigastric region), individual T1-weighted scans with a voxel size of 1.875 × 1.875 × 6.000 mm (TR = 460 ms, TE = 14 ms, image matrix = 256 × 256 × 40) were obtained with subjects holding their breath.

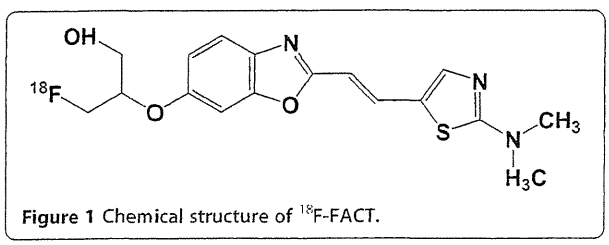

Figure 1 Chemical structure of ^{18}F-FACT.

Dosimetry

The Medical Internal Radiation Dose committee of the Society of Nuclear Medicine developed the algorithm to calculate absorbed dose D (the energy deposited per unit mass of medium (Gy)) in organs. The basic idea is that radiation energy from the radioisotope in the source organ is absorbed in the target organs, and the algorithm requires the net accumulated radioactivity in source organs as an input [15]. A PET scan contributes to quantitative knowledge on the whole-body distribution of radioisotope. In the present study, the accumulated activity in source organs was derived from PET measurements and the organ volumes of the reference male or female. The mean absorbed dose to the kth target organ is defined as follows:

$$\bar{D}(r_k) = \sum_h \tilde{A}_h \times S(r_k \leftarrow r_h) = \sum_h A_0 \times \tau_h \times S(r_k \leftarrow r_h),\ \tau_h = \frac{\tilde{A}_h}{A_0} \quad (1)$$

where $S(r_k \leftarrow r_h)$ is the absorbed dose in the kth target organ per unit of accumulated activity in the hth source organ, called the S value. $\tilde{A}_h$ is the number of disintegrations in the hth source organ, A_0 is the injected dose, and τ_h is the time-integrated activity coefficient in the hth source organ (equal to the number of disintegrations per unit activity administered). The effective dose E (Sv), as defined by the International Commission on Radiological Protection (ICRP) 60 [10], was obtained using the following equation:

$$E = \sum_i Q \times w_i \times D_i \quad (2)$$

where D_i is the absorbed dose of the ith target organ, w_i is the weighting risk factor in the ith target organ, and Q is the quality factor (Q = 1 for β- and γ-rays).

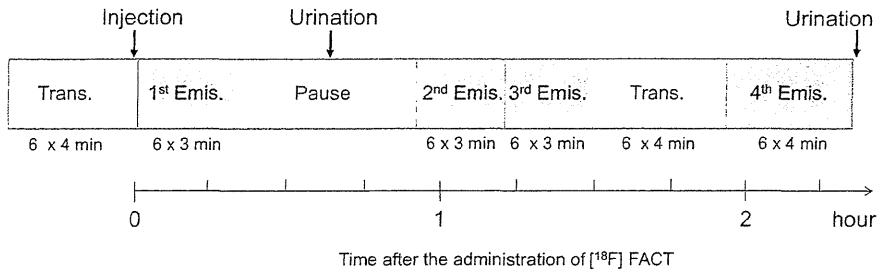

Figure 2 Overview of PET scan protocols. Four emission scans and two transmission scans (before and intermediate emission scans) with a $^{68}Ge/^{68}Ga$ source were performed. In particular, the second transmission scan was performed using a post-injection transmission scan.

Regions of interest

The number of source organs used for region-of-interest (ROI) drawing was 19 for male and 20 for female subjects. A detailed list of source organs is shown in Table 2. Two nuclear medicine physicians manually drew the ROIs using PMOD version 3.1 (PMOD Technologies, Zurich, Switzerland). All individual PET images and MRI images were co-registered to the first individual PET images using a rigid matching module of the same PMOD with a dissimilarity function of normalised mutual information (for MRI-to-PET cases) and the sum of the absolute difference (for PET-to-PET cases) algorithms.

For visceral organs with extremely high uptake (liver and gallbladder), individual ROIs were defined at a fixed

Table 2 [^{18}F]FACT time-integrated activity coefficients in the source organs

Organ	Human (MBq-h/MBq)							Mouse (MBq-h/MBq)
	Mean ± 1 SD	Subject 1	Subject 2	Subject 3	Subject 4	Subject 5	Subject 6	
Adrenal gland	5.38E−04 ± 2.98E−04	9.40E−04	8.40E−04	5.20E−04	3.70E−04	4.00E−04	1.60E−04	-
Brain	4.20E−02 ± 8.44E−03	5.41E−02	3.68E−02	3.53E−02	4.87E−02	4.42E−02	3.26E−02	6.99E−03
Breast	8.40E−03 ± 4.37E−03	1.14E−03	8.25E−03	5.59E−03	1.16E−02	1.19E−02	1.19E−02	-
Gallbladder content[a]	2.22E−01 ± 1.05E−01	-	1.49E−01	2.27E−01	3.88E−01	1.16E−01	2.31E−01	-
Lower large intestine content	2.12E−02 ± 2.03E−02	5.91E−02	1.06E−02	4.80E−03	2.27E−02	2.40E−02	5.96E−03	-
Small intestine content	8.78E−02 ± 1.08E−01	7.40E−02	3.74E−02	3.34E−02	3.06E−01	3.36E−02	4.25E−02	1.22E−01
Stomach content	6.71E−03 ± 2.28E−03	5.22E−03	6.23E−03	9.29E−03	9.84E−03	4.78E−03	4.87E−03	-
Upper large intestine content	2.55E−02 ± 1.89E−02	1.48E−02	4.88E−02	1.01E−02	4.99E−02	2.04E−02	8.85E−03	-
Heart content	1.12.E−02 ± 1.51E−03	1.24E−02	1.13E−02	1.02E−02	1.30E−02	1.15E−02	8.83E−03	3.95E−03
Heart wall	7.50E−03 ± 1.84E−03	4.63E−03	1.00E−02	8.84E−03	6.75E−03	7.28E−03	7.49E−03	2.39E−03
Kidney	1.34E−02 ± 3.27E−03	1.32E−02	1.16E−02	1.53E−02	1.89E−02	9.59E−03	1.20E−02	9.34E−03
Liver	4.92E−01 ± 1.05E−01	6.28E−01	5.85E−01	4.34E−01	5.15E−01	3.42E−01	4.49E−01	1.69E−01
Lung	3.55E−02 ± 1.16E−02	3.78E−02	5.31E−02	4.36E−02	2.46E−02	2.33E−02	3.08E−02	1.17E−02
Muscle	4.66E−01 ± 3.73E−01	9.43E−01	5.47E−01	7.97E−01	5.40E−02	4.12E−01	4.34E−02	1.57E−01
Ovary[b]	5.53E−04 ± 3.79E−05	-	-	-	5.70E−04	5.10E−04	5.80E−04	-
Pancreas	4.13E−03 ± 9.75E−04	6.10E−03	3.62E−03	3.93E−03	3.81E−03	3.55E−03	3.76E−03	-
Red marrow	3.98E−02 ± 4.33E−03	4.02E−02	3.83E−02	3.79E−02	4.59E−02	4.29E−02	3.34E−02	1.61E−02
Spleen	5.41E−03 ± 1.74E−03	8.64E−03	4.88E−03	3.83E−03	6.01E−03	4.77E−03	4.30E−03	1.28E−03
Testis[c]	5.77E−04 ± 4.67E−04	7.00E−04	6.10E−05	9.70E−04	-	-	-	-
Thyroid	3.53E−04 ± 1.55E−04	6.30E−04	3.70E−04	3.60E−04	2.40E−04	1.80E−04	3.40E−04	-
Urinary bladder contents	2.26E−02 ± 8.36E−03	1.70E−02	2.69E−02	1.55E−02	3.63E−02	2.49E−02	1.51E−02	6.56E−02
Uterus/uterine wall[b]	4.46E−03 ± 1.90E−03	-	-	-	6.42E−03	2.63E−03	4.33E−03	-
Remainder of the body	1.17 ± 3.63E−01	7.24E−01	1.06	9.48E−01	1.08	1.51	1.69	2.08

Averaged time-integrated activity coefficient (MBq-h/MBq) for the source organs (n = 6) from the whole-body PET data (n = 6) from experiments involving human subjects of [^{18}F]FACT and mice of [^{18}F]FACT. [a]Averaged value among five subjects excluding subject no. 1. [b]Average time-integrated activity coefficient among female subjects (n = 3). [c]Average time-integrated activity coefficient among male subjects (n = 3).

emission scan with about a 40% threshold against the maximum counts (first emission for the liver and third or fourth emission for the gallbladder). Then the ROI was applied to the other emission images with minor adjustment of its location or shape. For the intestines, if specific high uptake was observed, individual ROIs were defined on each time frame of the PET images with about a 10% threshold. If there was no specific high uptake in the intestines, and uptake could be regarded as uniform, individual ROIs were drawn around the corresponding area.

In order to obtain a typical radioactivity concentration within organs with less location mismatch between PET and the co-registered MRI images (brain, breast, heart wall, heart contents, kidney, liver, lung, muscle, bones, spleen and thyroid), individual ROIs were drawn on co-registered MRI images. For other low-uptake organs (adrenal gland, stomach contents, pancreas, ovary, uterus and testis), individual ROIs were drawn on each time frame of the PET images and referred to the co-registered MRI images. To avoid a partial volume effect, the size of the ROI for these MRI available organs was made slightly smaller than the entire source organ. It should also be noted that all activities in vertebrae ROIs was assumed to be in the red marrow in the present study.

Data analysis

Averaged time-activity curves for each organ were obtained using the ROI values from each subject's PET images. Because the PET images were decay-corrected at the start of each scan during the reconstruction procedure, the non-decay-corrected time-activity curves (C(t), Bq/ml) were re-calculated. During each whole-body emission scan, the bed position was moved from the foot to the head (six bed positions in total). However, we assumed that PET counts at all bed positions were acquired at the mid-scan time. Then, individual radioactivity concentration per injected dose A_0 (Bq) was extrapolated into the percent injected dose (%ID) of the reference subject as follows:

$$\%\mathrm{ID}(t)_{\mathrm{reference}} = \left(\frac{C(t)}{A_0}\right)_{\mathrm{individual}} \times V_{\mathrm{reference}} \qquad (3)$$

where V (ml) is the organ volume, and $V_{\mathrm{reference}}$ is V of the reference subject (we used a 70-kg adult male and 58-kg adult female as the male and female reference subjects) [16,17]. Even though some organs such as the intestine may change their volume over time, we used the reference subjects' organ volumes over the time period of the calculation of the %ID.

The time-integrated activity coefficient τ (Bq-h/Bq) in Equation 1 was obtained by fitting (%ID(t)) using a mono-exponential function and integrating from time zero to infinity. If the time-activity curve did not converge at the last PET scan (e.g. intestines and gallbladder), time-activity curves were fitted using two exponential functions, and then the area under the curve after the acquisition of the last image was calculated by assuming only physical decay of ^{18}F and no additional biologic clearance to be conservative [10]. The time-integrated activity coefficient for urinary bladder content was calculated by applying the dynamic urinary bladder model [10] to the urine samples with a bladder voiding interval of 2 h. The decay-corrected cumulative activity for urine was fitted using the equation $A \times (1 - \exp(-\ln(2) \times t / \tau))$, where τ is the biological decay and A is the fraction of activity released from the body. The sum of the time-integrated activity coefficient for the specific organs was subtracted from the time-integrated activity coefficient for the total body, which was calculated from the time integral of the decaying injected radioactivity. Then the residual of the subtraction was regarded as the time-integrated activity coefficient in the remainder of the body. All fitting procedures were undertaken using a mean fit of R^2 of 0.93 ± 0.13.

Finally, the time-integrated activity coefficient τ (Bq-h/Bq) was used to calculate the absorbed dose, D, in Equation 1 and the effective dose, E, in Equation 2. Both kinetics calculations (fitting and integration) and dose estimation were performed using OLINDA/EXM software version 1.0 (Department of Radiology and Radiological Sciences Vanderbilt University, Nashville, TN, USA) [17].

Animal experiments

The experimental protocols were reviewed by the Committee on the Ethics of Animal Experiments at Tohoku University School of Medicine and performed in accordance with the Guidelines for Animal Experiments issued by the Tohoku University School of Medicine. Estimated radiation dose of [^{18}F]FACT in the human subjects calculated from mouse data sets was compared with those of [^{18}F]FACT from human whole-body PET scans. An average dose of 1.4 MBq of [^{18}F]FACT was intravenously injected into ICR mice (age, 6 weeks; average body weight, 30 g) without anaesthesia. In the [^{18}F]FACT study, the mice were killed by cervical luxation at 2, 10, 30, 60 and 120 min ([^{18}F]FACT) after administration (n = 4 at each time point). The masses of the blood, heart, lung, liver, spleen, small intestine, kidney, brain and urine samples were measured, and activity was also measured using a well counter. Thigh bone and muscle were also sampled. The average uptake of the

radioligand into the male reference subject (70 kg) was extrapolated as follows [18]:

$$\%\mathrm{ID}(t)_{\mathrm{human}} = \left(\frac{\%\mathrm{ID}(t)}{\mathrm{mass}_{\mathrm{organ}}}\right)_{\mathrm{mouse}} \times \left(\mathrm{mass}_{\mathrm{body}}\right)_{\mathrm{mouse}} \times \left(\frac{\mathrm{mass}_{\mathrm{organ}}}{\mathrm{mass}_{\mathrm{body}}}\right)_{\mathrm{human}} \quad (4)$$

where the bodyweight of the mouse was assumed to be 30 for [^{18}F]FACT.

Finally, in the same manner as in the human PET data analysis, time-integrated activity coefficients, absorbed doses and effective doses were calculated using the OLINDA/EXM software version 1.0. Sampled blood, thighbone and urine were regarded as heart contents, red bone marrow and urinary bladder contents, respectively.

Results and discussion

Biodistribution of [^{18}F]FACT

Figure 3A is the coronal PET image for a single female subject (no. 5) and demonstrates the typical biodistribution of [^{18}F]FACT in the human body. The highest accumulations of this radioligand were observed in the gallbladder, liver, intestine and urinary bladder. For subject no. 1, [^{18}F]FACT contained in the bile was excreted from the liver to the duodenum through the biliary tract (Figure 3B). The biodistribution pattern of [^{18}F]FACT in human subjects showed a predominant hepatobiliary excretion, which is similar to what has been observed for other amyloid ligands, such as [^{11}C]PIB, [^{18}F]AV-45, [^{18}F]GE067 and [^{18}F]BAY94-9172 [7,8,10,11].

Figure 4 shows the decay-corrected time-activity curve of the %ID for typical source organs (brain, liver, spleen, lung, kidney, heart content, heart wall, muscle, red marrow, small intestine contents, gallbladder, upper large intestine contents and urinary bladder) from the six volunteers and the mice experiments. A significant difference between the %ID from humans and mice was observed in the brain, liver, spleen, heart contents, red marrow and urinary bladder, and these differences propagated the different results regarding dose estimation. In human subjects, ^{18}F uptake in the gallbladder contents and the intestines (Figure 4J,K,L) indicated larger individual variations in radioactivity uptake relative to other organs (e.g. the kidney as shown in Figure 4E). Radioactivity uptake in the upper large intestine showed propagation of both ligand kinetics and inter-subject variation from the gallbladder (Figure 4K,L). Scheinin et al. previously reported that inter-subject variation in ligand uptake ([^{11}C]PIB) in the gallbladder may be due to the quality and quantity of post-injection food intake [7]. In the present study, the subjects drank water during the interval between the first and second PET scans. This may have been responsible for the increase in inter-subject variation regarding the gallbladder. Furthermore, because the gallbladder uptake in some subjects had declined or remained at a low level at the final time points, we assumed that there was only physical radioactive decay after the last PET scans. However, this assumption may have led to a conservative estimation of the absorbed dose.

Figure 5 presents typical brain PET images obtained using [^{18}F]FACT at different time points with an

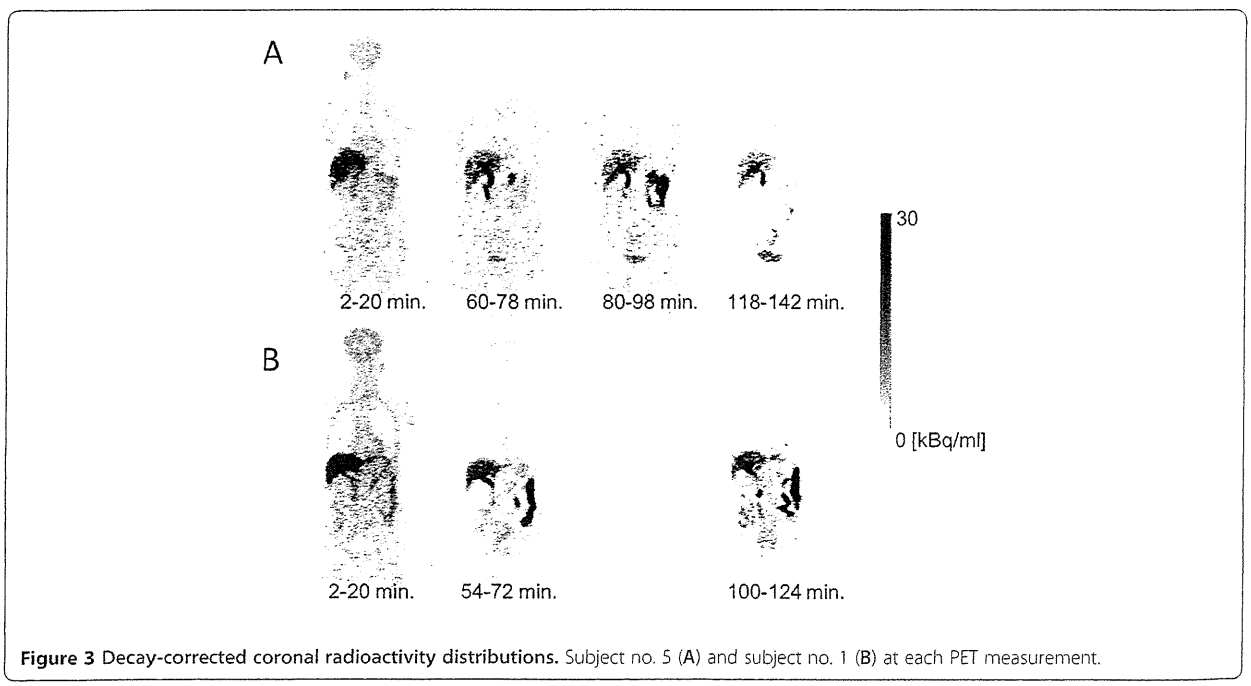

Figure 3 Decay-corrected coronal radioactivity distributions. Subject no. 5 (A) and subject no. 1 (B) at each PET measurement.

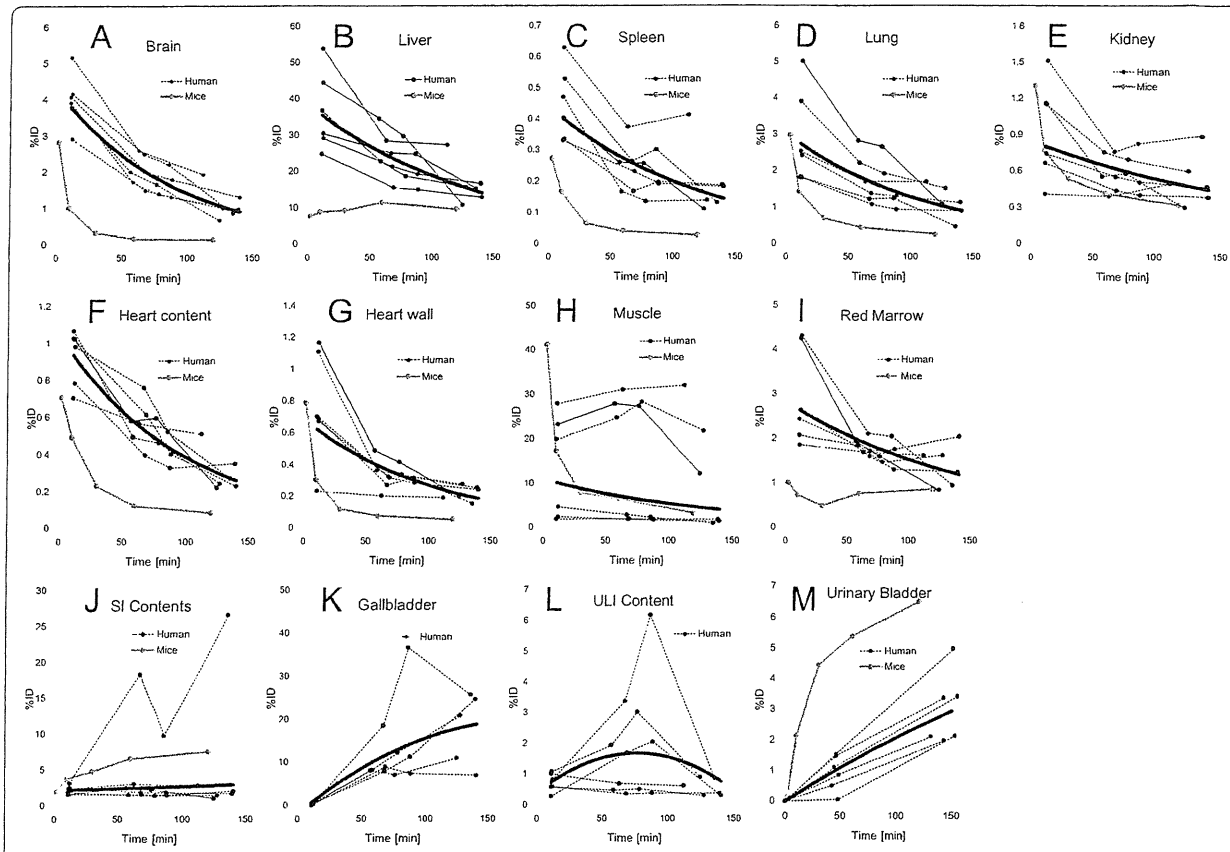

Figure 4 Decay-corrected time-activity curves of %ID. (**A**) Brain, (**B**) liver, (**C**) spleen, (**D**) lung, (**E**) kidney, (**F**) heart content, (**G**) heart wall, (**H**) muscle, (**I**) red marrow, (**J**) SI contents, (**K**) gallbladder, (**L**) ULI content and (**M**) urinary bladder for individual human (dashed black line) and averaged mice extrapolation (n = 4 at each time point, grey line). The solid black line indicates fitted curve using exponential function from all subjects' data points. The urinary bladder curve indicates accumulated activity excreted at all voiding/sampling moments.

acquisition time of 3 min (first, second and third emission) and 4 min (fourth emission). There was no significant retention of [^{18}F]FACT in the brain, and this may have been because the subject was normal.

Estimated dose of [^{18}F]FACT

The [^{18}F]FACT time-integrated activity coefficients in the source organs are shown in Table 2, and the absorbed doses are shown in Table 3. The averaged time-integrated activity coefficient for the gallbladder, as shown in Table 2, was calculated among five subjects excluding subject no. 1; however, in the case of the averaged absorbed and effective doses, subject no. 1 was included (Table 3).

High absorbed dose in humans was observed in the gallbladder (333 ± 251 μGy/MBq), liver (77.5 ± 14.5 μGy/MBq), small intestine (33.6 ± 30.7 μGy/MBq), upper large intestine (29.8 ± 15.0 μGy/MBq) and lower large intestine (25.2 ± 12.6 μGy/MBq). In mice, high absorbed doses were observed in the small intestine (38.5 μGy/MBq), liver (25.5 μGy/MBq) and urinary bladder wall (43.1 μGy/MBq) for [^{18}F]FACT (Table 3).

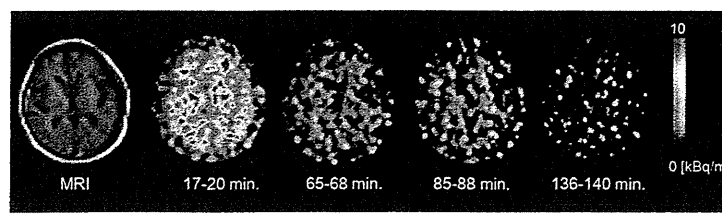

Figure 5 Decay-corrected brain PET images of subject no. 3 at different time points.